A TiO_2/FeMnP Core/Shell Nanorod Array Photoanode for Efficient Photoelectrochemical Oxygen Evolution

Desmond E. Schipper,[†,‡] Zhenhuan Zhao,[†,§,Δ] Andrew P. Leitner,[‡] Lixin Xie,[Ω] Fan Qin,[Δ] Md Kamrul Alam,[Δ] Shuo Chen,[Ω] Dezhi Wang,[Ω] Zhifeng Ren,[Ω] Zhiming Wang,[§] Jiming Bao,[, §,Δ] and Kenton H. Whitmire[‡,*]*

[‡] Department of Chemistry, MS60, Rice University, 6100 Main Street, Houston, Texas 77005, United States

Email: whitmir@rice.edu, jbao@central.uh.edu

[§] Institute of Fundamental and Frontier Sciences, University of Electronic Science and Technology of China, Chengdu 610054, China

[Δ] Department of Electrical and Computer Engineering, University of Houston, Houston, Texas 77204, United States

[Ω] Department of Physics & Texas Center for superconductivity of the University of Houston, University of Houston, Houston, Texas 77204, United States

[†]These authors contributed equally.

Abstract: A variety of catalysts have recently been developed for electrocatalytic oxygen evolution, but very few of them can be readily integrated with semiconducting light absorbers for photoelectrochemical or photocatalytic water splitting. Here, we demonstrate an efficient core/shell photoanode with a highly active oxygen evolution electrocatalyst shell (FeMnP) and semiconductor core (rutile TiO_2) for photoelectrochemical oxygen evolution reaction (PEC-OER). Metal-organic chemical vapor deposition (MOCVD) from a single-source precursor was used to ensure good contact between the FeMnP and the TiO_2. The TiO_2/FeMnP core/shell photoanode reaches the theoretical photocurrent density for rutile TiO_2 of 1.8 mA cm^{-2} at 1.23 V *vs* RHE under simulated 100 mW cm^{-2} (1 sun) irradiation. The dramatic enhancement is a result of the synergistic effects of the high OER activity of FeMnP (delivering an overpotential of 300 mV with a Tafel slope of 65 mV dec^{-1} in 1 M KOH) and the conductive interlayer between the surface active sites and semiconductor core which boosts the interfacial charge transfer and photocarrier collection. The facile fabrication of the TiO_2/FeMnP core/shell nanorod array photoanode offers a compelling strategy for preparing highly efficient photoelectrochemical solar energy conversion devices.

KEYWORDS: solar water splitting, core-shell nanorod, titanium dioxide, FeMnP, metal-organic chemical vapor deposition, electrocatalysis

Solar-driven water splitting, which cleanly converts solar energy to chemical energy in the form of hydrogen, holds the promise of meeting the world's clean energy demands.[1] There are three approaches to use solar energy for the production of fuels from water: photovoltaic-electric (PV-E), photoelectrochemical (PEC), and photocatalytic water splitting,[2] although many semiconductors alone can in principle perform PEC or photocatalytic water splitting.[3] It is well understood now that semiconductors should be integrated with hydrogen and oxygen evolution catalysts to achieve stable and efficient solar water splitting.[4] As such, the development of highly active catalysts to pair with semiconductors is essential to achieving efficient solar water splitting. Recent years have witnessed great progress in the development of water-splitting electrocatalysts composed of earth-abundant elements,[5-9] predominantly for the oxygen evolution reaction (OER) as it is more kinetically demanding than the hydrogen evolution reaction (HER).[10,11]

Transition metal phosphides (TMPs) have gained eminence as the next-generation water splitting catalysts with high activity demonstrated for both HER and OER.[12-15] Binary phosphides such as Ni_2P,[16] FeP,[17-19] CoP,[20–22] WP and MoP,[23] and recently ternary bimetallic phosphides such as CoMnP,[24] $(Co_{0.52}Fe_{0.48})_2P$,[25] MoWP,[23] and NiCoP[26,27] have shown higher activities than transition metal chalcogenides and double-metal hydroxides with ternary TMPs exhibiting lower overpotentials than binary TMPs. To date, there has been no report of the integration of TMPs with a semiconductor light absorber for PEC-OER. Previous reports are mainly focused on the integration of metal oxide/hydroxide OER catalysts with a semiconductor photoanode,[28] such as CoPi sensitized WO_3 and $BiVO_4$,[29,30] CoPi and hydroxide decorated hematite,[31,32] and nickel oxide modified silicon;[33] however, the respective performances of these materials are unsatisfactory because of their relatively low OER catalytic activity and because

the poor electrical conductivities of metal oxides/hydroxides limits the charge transfer between the semiconductor and OER catalysts, resulting in the high interfacial recombination of photocarriers.

The interfacial kinetics and underlying mechanism of such systems have been systematically investigated and useful models have been established for the understanding of interfacial charge separation and charge transfer,[34,35] which should guide the design and construction of reasonable photoelectrodes for PEC. TMPs typically have a metallic nature and the introduction of TMPs to the surface of semiconductors should promote the interfacial charge transfer and charge transportation from the semiconductor to the active surface, which leads to high PEC performance. However, current synthetic methods are not suitable for pairing a TMP with a semiconductor.

Recent work in our laboratory has shown that designer organometallic precursors can be converted to specific metal phosphide materials by metal-organic chemical vapor deposition (MOCVD) under mild conditions,[36–38] a strategy that is ideally suited to grow specific TMPs directly on semiconductors without compromising the substrate. Moreover, because the stoichiometry is built into the precursor, the method can scale without the inhomogeneity of phases expected from existing approaches. Herein, we report a ternary TMP catalyst, FeMnP, synthesized *via* MOCVD from the single-source precursor $FeMn(CO)_8(\mu\text{-}PH_2)$.[39] FeMnP was deposited on a three-dimensional TiO_2 nanorod array photoanode to form a TiO_2/FeMnP core/shell nanostructure. As a result, dramatically enhanced PEC performance was achieved with the core/shell nanorod array photoanode. The high PEC performance is ascribed to the high OER catalytic activity, high conductivity of FeMnP, and the excellent interface with TiO_2, providing rapid charge transfer and separation without creating non-radiative recombination centers. As a

result, the theoretical maximum photocurrent for TiO_2 is achieved.[40] Furthermore, the method can be considered general; other precursors sourced from the vast catalog of known main group element-containing homo- and heterometallic carbonyl clusters will be used to deposit specific electrocatalysts onto semiconductors.[41] This works describes a method of device and material engineering for highly efficient solar water splitting.

RESULTS AND DISCUSSION

The TiO_2 nanorod arrays on fluorine doped tin oxide (FTO) were grown by a hydrothermal method.[42] The TiO_2/FeMnP core/shell nanorod array was then fabricated by the MOCVD method using single-source precursor $FeMn(CO)_8(\mu\text{-}PH_2)$ with a home-made apparatus (**Figure S1**).[36] The core/shell nanostructure was first confirmed by scanning electron microscopy (SEM) in **Figure 1a and b**. After FeMnP deposition, the smooth surface of TiO_2 nanorod (**Figure S2**) had been uniformly coated by an FeMnP film consisting of numerous nanocrystals. The strong peak located at 2θ of 39.9° in the X-ray diffraction (XRD) pattern of TiO_2/FeMnP is assigned to the (111) plane of hexagonal FeMnP (**Figure S3**), and the peaks located at 33.5°, 51.4°, and 62.5° belong to the rutile TiO_2 nanorods (JCPDS No. 21-1276),[42] confirming the successful deposition of FeMnP on TiO_2. The broadness of the FeMnP (111) peak indicates the crystallite size is small, consistent with the observed nanocrystals of FeMnP on the TiO_2 surface from the SEM image (**Figure 1b**). Furthermore, we used high-resolution transmission electron microscopy (HRTEM) to examine the crystalline structure. As we can see from **Figure 1c**, the FeMnP shell is clearly seen to be crystalline with exposed (111) and (001) planes given the d-spacings of 0.23 nm and 0.35 nm of the crystalline lattice, respectively. The insert FFT image also confirmed the (111)

and (001) planes. The FeMnP shell thickness is measured to be 18 nm. The TEM image in **Figure 1d** also clearly shows a core/shell structure. To probe the elemental composition of the core/shell, energy dispersive spectroscopy (EDS) mapping under TEM was conducted over a single TiO_2/FeMnP core/shell nanorod. As show in **Figure 1e**, Ti and O are located in the central part of the core/shell nanostructure, while the elements Fe, Mn, and P are homogeneously distributed across the whole nanorod, confirming the core/shell nanostructure.

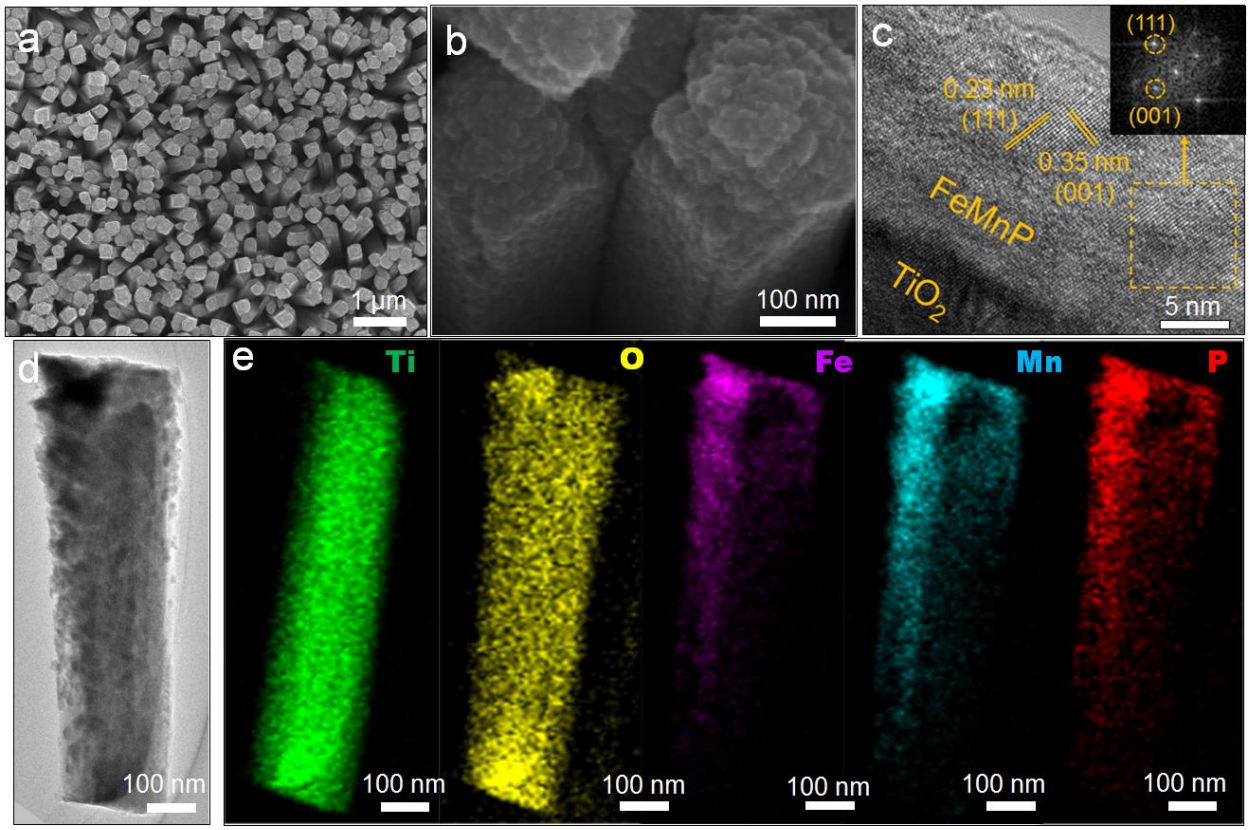

Figure 1. Structural characterization of TiO_2/FeMnP core/shell nanorod array. (a) and (b) SEM images at different magnifications. (c) HRTEM image showing the thickness of FeMnP shell and the crystalline lattice on TiO_2. The insert is the fast Fourier transform (FFT) pattern of the selected area. (d) TEM image showing the uniform coating of FeMnP on a TiO_2 nanorod. (e) EDS mapping over a single TiO_2 nanorod showing the distribution of Fe, Mn and P.

Sputtering assisted X-ray photoelectron spectroscopy (XPS) is an effective method to analyze the depth dependent element composition. We conducted sputtering assisted XPS analysis with our fresh TiO_2/FeMnP core/shell sample (**Figure 2**). At the surface, Fe and Mn were in the zero-oxidation ($2p_{3/2}$ = 706.7 eV) and 2^+ oxidation state ($2p_{3/2}$ = 641.4 eV),[43,44] respectively. There is a small amount of zero-oxidation state of Mn at the surface, giving the weak peak at 638.7 eV. The P 2*p* core level spectrum showed two different oxidation states with one stronger peak at 129 eV corresponding to the phosphide component, and one weaker peak at 132.6 eV corresponding to the oxidized phosphorous component, which is common in metal phosphides.[18] A large shift in the $Mn2p_{3/2}$ binding energy toward 638.7 eV indicated the Mn was mostly zero-valent after three minutes of sputtering. All of the Fe and P was zero-valent. Increasing the sputtering time to 6 min, the peak intensity at 638.7 eV increased, corresponding to an increase of metallic Mn. The atomic ratio of Fe:Mn:P was 1.4:1:1 with a slight increase of Fe suggesting preferential sputtering of the Mn and P.[45-50] The results of sputtering assisted XPS analysis indicated the FeMnP shell is metallic.

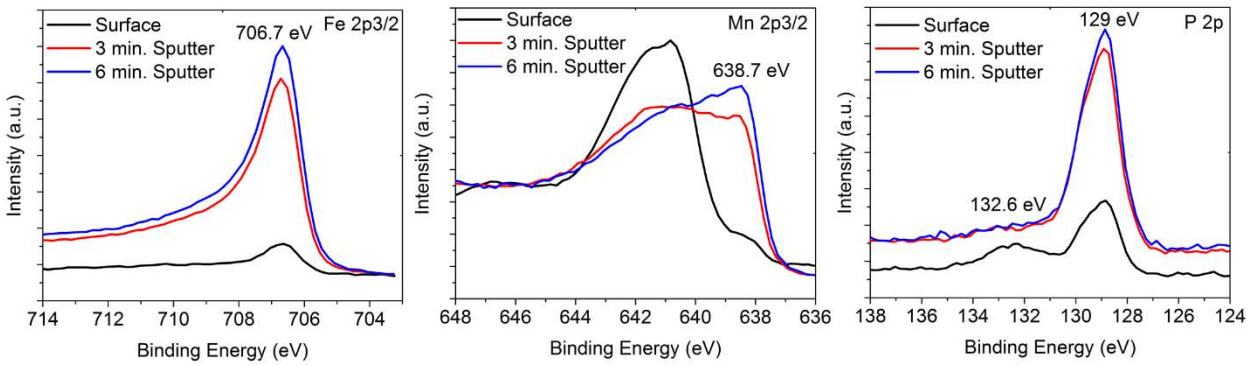

Figure 2. Chemical composition and states of the FeMnP shell in the TiO_2/FeMnP core/shell nanostructure showing the XPS spectra for Fe $2p_{3/2}$, Mn $2p_{3/2}$ and P 2p orbitals, respectively.

The electrocatalytic activity of FeMnP supported on FTO (fluorine-doped tin oxide glass) by the same MOCVD method was studied *via* a standard three-electrode configuration in 1.0 M KOH. Before the electrochemical measurements, FeMnP on FTO was characterized by SEM, XRD, and TEM. SEM shows that FeMnP on FTO exhibits a uniform nanoplate structure (**Figure 3a**). XRD data also confirmed FeMnP is in its hexagonal setting with the strong peak at 2θ of 39.9° corresponding to the (111) plane, and the weak peaks at 25.2° and 51.9° indexed to the (001) and (002) plane, respectively (**Figure S4**). The HRTEM image in **Figure 3b** shows a clear crystalline lattice with a d-spacing of 0.23 nm, which is indexed to the (111) plane. It is therefore concluded that the FeMnP nanoplates on FTO substrate have the same crystalline structure as the FeMnP shell on the TiO_2 nanorods.

Figure 3c shows the polarization curves after iR-correction of the FeMnP/FTO and bare FTO electrodes. The FeMnP nanoplates exhibit excellent OER activity, as demonstrated by the low onset overpotential (240 mV, J = 1.0 mA cm^{-2}) and small overpotential of 300 mV to reach an electrocatalytic current density of 10 mA cm^{-2}. The high electrocatalytic OER activity was also confirmed by the low Tafel slope of 65 mV dec^{-1}. In addition, FeMnP has excellent stability given that the CV profile in the 1st cycle is identical with that of the 1000th cycle at the high scan rate of 100 mV s^{-1} (**Figure 3d**). Compared to other catalysts (**Table S1**), the OER performance of FeMnP is much better than manganese oxide-based OER catalysts,[51-53] nanostructured cobalt oxide/selenide OER catalysts,[54-56] and NiO_x and CoPi.[57] The high OER performance of FeMnP is helped by the small charge transfer resistance (**Figure S5**) and large electrocatalytically active surface area (ECSA) which is linearly related to the double-layer capacitance (C_{dl}). The C_{dl} of FeMnP/FTO is calculated to be 15.9 mF cm^{-2}, almost 192-fold higher than that of bare FTO (0.0829 mF cm^{-2}) (**Figure S6**). The Faradaic efficiency for the FeMnP/FTO electrode was

measured using an airtight electrochemical cell. Water electrolysis was performed at an overpotential of 300 mV in 1 M KOH using FeMnP/FTO and Pt as the working electrode and counter electrode, respectively. The experimentally produced O_2 was analyzed using gas chromatography (GC) which was calibrated with pure O_2 in advance. The experimentally produced amount of O_2 amount was close to the theoretical amount of O_2, giving the value for the Faradaic efficiency of 97% (**Figure S7**).

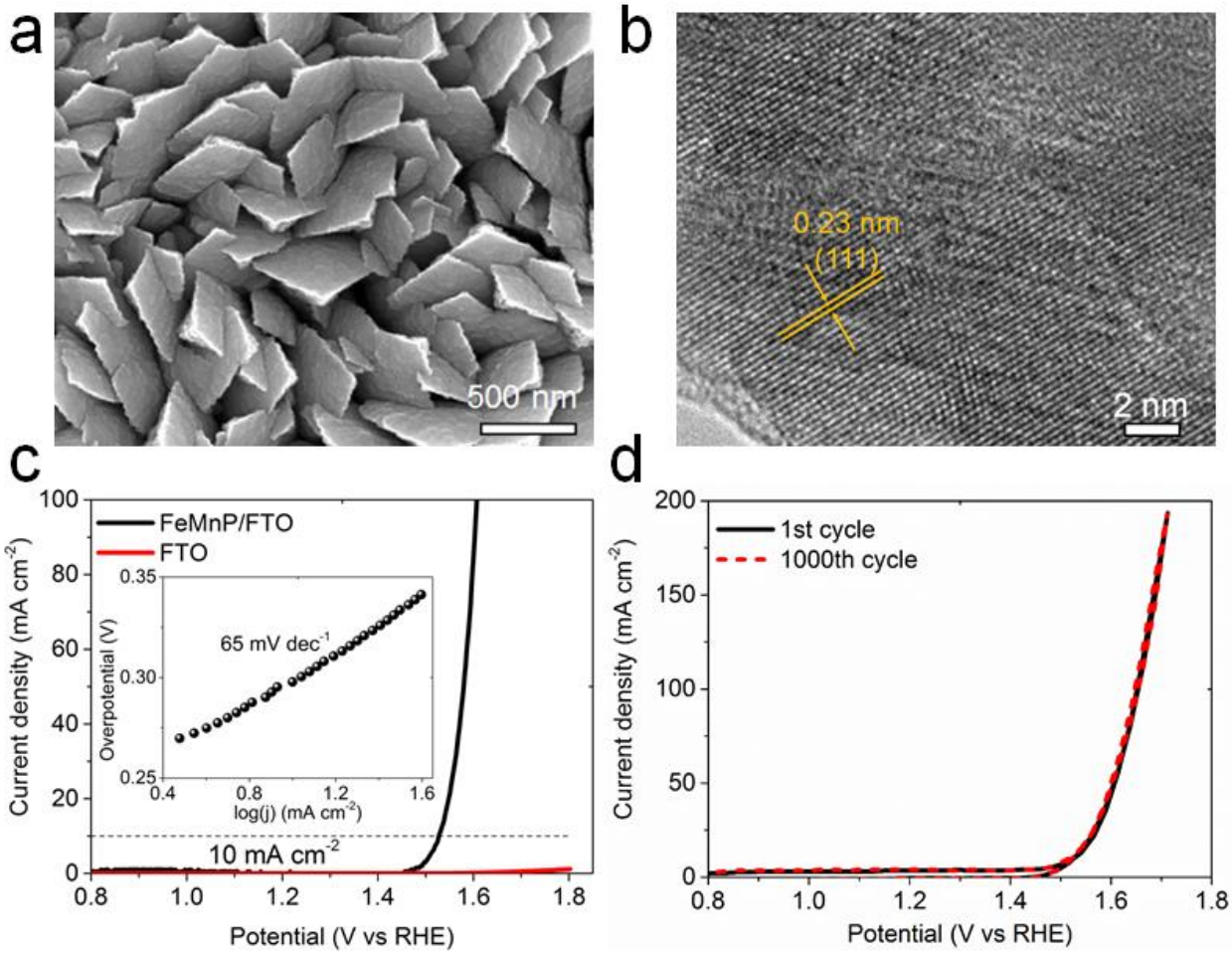

Figure 3. Morphology of the FeMnP on FTO anode and its OER characterizations. (a) SEM image of FeMnP on FTO and (b) HRTEM image. (c) Polarization curves of FeMnP/FTO and bare FTO electrodes in 1.0 M KOH at 10 mV s^{-1}. The insert refers to the corresponding Tafel

plot of FeMnP/FTO. (d) CV curves of FeMnP/FTO electrode for the 1st cycle and the 1000th cycle at scan rate of 100 mV s^{-1}.

The optical properties of the TiO_2 nanorods on FTO and the TiO_2/FeMnP core/shell nanostructures on FTO were analyzed by UV-vis spectroscopy. The light absorption edge of rutile TiO_2 nanorods was found to be about 400 nm, giving a 3.0 eV band gap (**Figure S8).** The TiO_2/FeMnP core/shell nanostructure displays very low transmittance at all wavelengths (**Figure S9**). Therefore, in this work, all the PEC measurements were conducted with the light irradiation from the uncoated backside. Then the PEC OER performance of TiO_2/FeMnP core/shell nanostructure photoanode was evaluated in a three-electrode configuration in 1.0 M NaOH under simulated 1 Sun irradiation using an AM 1.5G filter (100 mW cm^{-2}) from the backside. It was found that the TiO_2/FeMnP core/shell photoanode displayed a significantly enhanced photocurrent density (**Figure 4a**). The TiO_2 nanorod photoanode displayed a current density of 0.7 mA cm^{-2} at 1.23 V *vs* RHE under irradiation, similar to previous reports.[42] Surprisingly, the TiO_2/FeMnP core/shell nanostructure photoanode displayed a much higher current density of about 2.9 mA cm^{-2} at 1.23 V *vs* RHE, an almost 4-fold enhancement. By subtracting the dark current density, the photocurrent density was about 1.8 mA cm^{-2}, very close to the theoretical photocurrent density of rutile TiO_2 under 100 mW cm^{-2} light irradiation.[40] The photocurrent density of the present TiO_2/FeMnP core/shell photoanode is higher than those of all reported TiO_2 based photoanodes in **Table S2**. Notably, The TiO_2/FeMnP core/shell nanostructure photoanode showed a large negative shift of about 200 mV of the onset potential of the photocurrent. The highest photoconversion efficiency (**Figure 4b**) of the bare TiO_2 nanorod photoanode was 0.25% at 0.65 V *vs* RHE, while at the same potential the photoconversion efficiency of the TiO_2/FeMnP core/shell photoanode increased to 0.65%, an almost 2.6-fold

enhancement. The maximum photoconversion efficiency was 1.33% at 0.95 V *vs* RHE for the TiO_2/FeMnP core/shell photoanode, while at the same potential the photoconversion efficiency of bare TiO_2 nanorod was only 0.17%. The photocurrent density is strongly dependent on the charge recombination rate. The transient photocurrent curve was obtained by chronoamperometry to investigate the charge recombination behavior (insert image in **Figure 4c**). Both the TiO_2 nanorod and TiO_2/FeMnP core/shell nanorod photoanodes showed fast responses to the switching of the light ON-OFF signal. A normalized parameter (*D*) was derived from the transient photocurrent curve to quantitatively measure the charge recombination behavior.[58] **Figure 4c** shows the normalized plots of ln D as a function of time (t). The transient time constant (*T*) is defined as the time when ln D = -1. *T* was estimated to be 4.6 s and 10.2 s for the TiO_2 and TiO_2/FeMnP core/shell nanorod arrays, respectively, which confirm the suppression of the charge recombination. The photochemical stability of the TiO_2/FeMnP core/shell nanorod photoanode was also investigated by conducting a chronoamperometry measurement at 1.23 V *vs* RHE under light irradiation (**Figure 4d**). Modest decay of the photocurrent density can be observed given that the photocurrent density decreased over the first 20 minutes of operation but remained nearly constant for the remainder of the test.

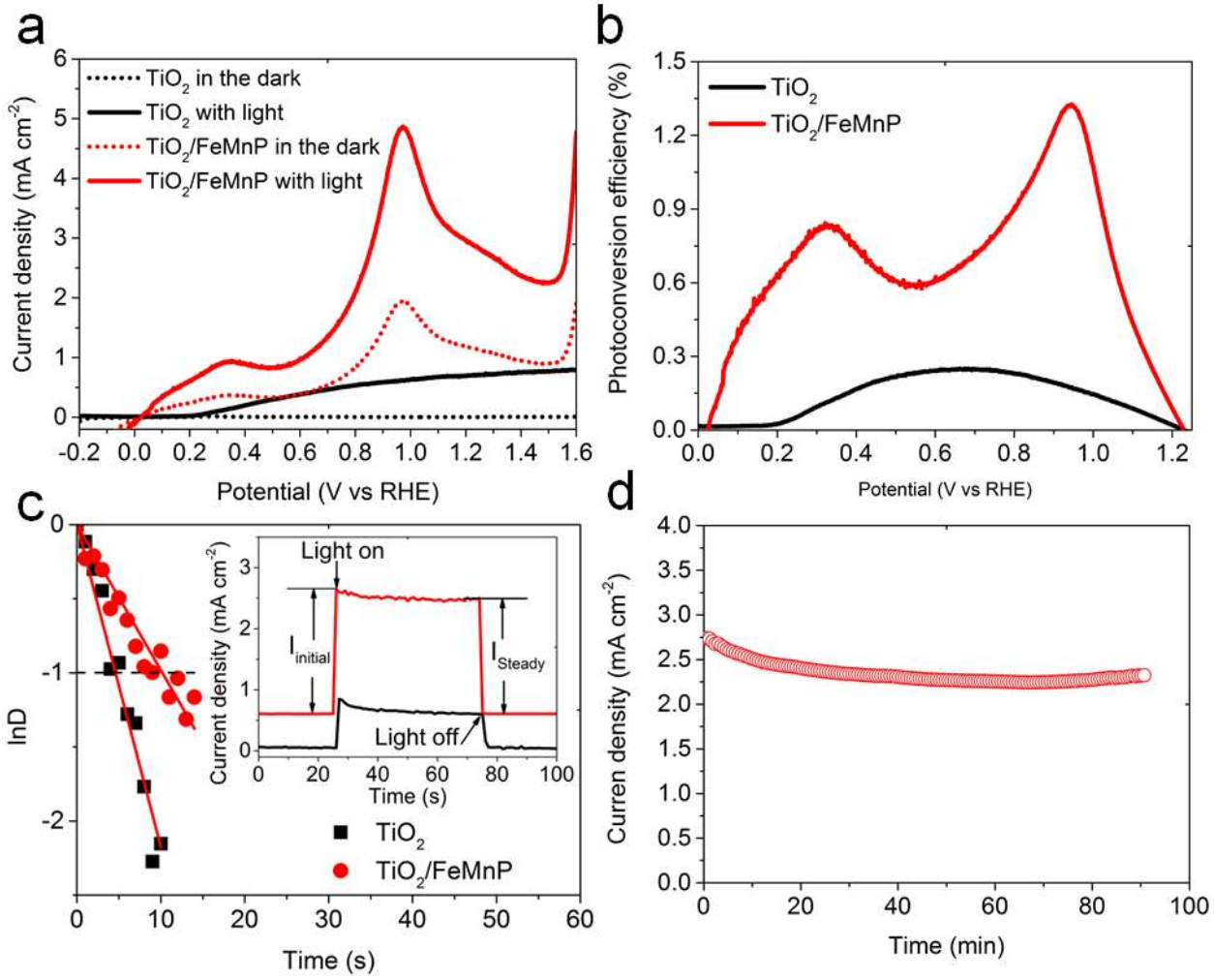

Figure 4. PEC-OER characterization. (a) *J-V* curves of TiO_2 nanorod and TiO_2/FeMnP core/shell nanorod photoanodes in the dark and under irradiation. (b) Photoconversion efficiency as a function of applied voltage. (c) Normalized plots of the photocurrent-time dependence for the pristine TiO_2 nanorods and TiO_2/FeMnP core/shell nanorods. The insert image refer to the on-off *J-t* curves of the TiO_2 and TiO_2/FeMnP core/shell nanorod at 1.23 V *vs* RHE. $D = (I_t - I_{steady}) / (I_{initial} - I_{steady})$. I_t, $I_{initial}$ and I_{steady} are the time-dependent, the initial photocurrent, and the steady state photocurrent. (d) Photochemical stability of the TiO_2/FeMnP core/shell nanorod photoanode at 1.23 V *vs* RHE.

Sputtering assisted XPS was used to analyze the chemical state of the TiO_2/FeMnP core/shell nanorod array after the 90 min stability test (**Figure S10**). The surface Fe and Mn were heavily oxidized to Fe^{3+} (711 eV) and Mn^{4+} (642.9 eV).[59,60] It is well accepted that metal phosphides can convert to metal hydroxides and oxyhydroxides, which are also highly active OER catalysts.[61] After several minutes of sputtering to remove the oxide layer, the existence of metallic FeMnP is confirmed with the peak at 706.9 eV in the Fe 2p3/2 spectra and the peak at 129.4 eV in the P 2p spectra, as well as the obvious negative shift from 642.9 eV to 641.9 eV of the Mn oxidization peak in its 2p3/2 spectra.

The presence of a metallic FeMnP interlayer promoted the charge transportation because of its high electrical conductivity and hence enhanced the charge separation, confirmed by the much smaller charge transfer resistance (**Figure S11**). As a result the carrier density was significantly increased for the TiO_2/FeMnP core/shell nanorod array compared to the bare TiO_2 nanorod array. **Figure 5a** shows the Mott-Schottky plots of the TiO_2 nanorod and TiO_2/FeMnP core/shell nanorod photoanodes in the dark. Using the slopes of the linear parts of the Mott-Schottky plots, the donor densities of the TiO_2 and TiO_2/FeMnP photoanodes were calculated to be 1.04×10^{18} cm^{-3} and 1.77×10^{20} cm^{-3}, respectively. The enhanced donor density contributed to the high PEC performance of the TiO_2/FeMnP core/shell nanorod. The flatband potential of TiO_2 nanorod was determined to be -0.81 V *vs* Ag|AgCl (-0.61 V *vs* NHE) at pH 13.6 in aqueous NaOH from the Mott-Schottky plots in **Figure 5a**. Considering 3.0 eV as the band gap of TiO_2, the valence band maximum (VBM) and conduction band minimum (CBM) were calculated to be -7.71 eV and -4.71 eV *versus* vacuum level, respectively. The measured work function of bare FTO and FeMnP/FTO was -5.17 eV and -5.25 eV (**Figure S12**), respectively. The measured work function of FTO matches with the value previously reported in the literature.[62] The work

function of FeMnP is very close to those of metal, confirming its metallic nature. The Fermi level of FTO is lower than the CBM of TiO_2, and on the other hand, the Fermi level of FeMnP is closer to the VBM of TiO_2. Based on these considerations, the band alignment is illustrated in **Figure 5b**. Under illumination, the photogenerated electrons in the CB of TiO_2 migrate to FTO and then to the counter electrode Pt for the water reduction reaction. The photogenerated holes in the VB of TiO_2 will flow to the metallic FeMnP interlayer and then to the oxide surface active sites for the water oxidation reaction.

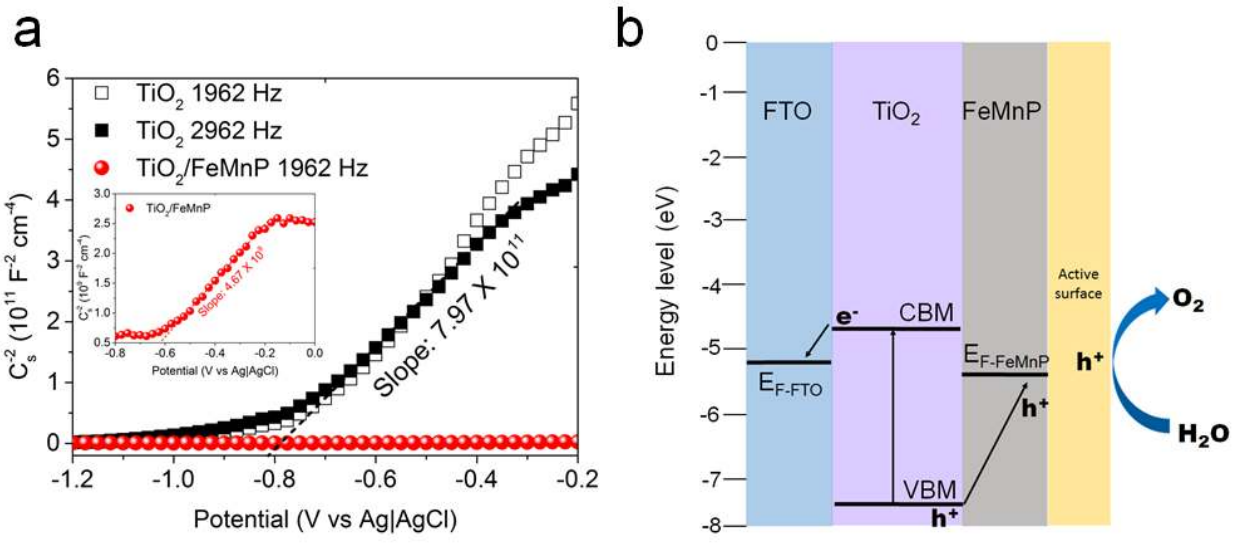

Figure 5. (a) Mott-Schottky plots of TiO_2 nanorod and TiO_2/FeMnP core/shell nanorod photoanodes in the dark. (b) Band alignment of TiO_2/FeMnP core/shell nanorod structure. $E_{F\text{-}FTO}$ and $E_{F\text{-}FeMnP}$ refer to the Fermi level of FTO and FeMnP.

Metal phosphides are known to convert to metal oxides and oxyhydroxides at their surfaces under aqueous conditions. In turn, these species are believed to be the active catalysts for the oxygen-evolution reaction.[61] From our XPS studies, it was determined that the surface after testing was primarily manganese (IV) oxo and hydroxo species with some iron (III) present coupled with a structural surface reorganization observed with SEM (**Figure S13**). The metal

responsible for the catalysis is not plainly clear. A recent study of 3d transition metal hydroxide/oxyhydroxide (M = Mn, Fe, Co, Ni) species towards OER found Fe-OOH to be most active with Mn-OOH being the least active;[63] thus, iron would appear to be the active species in the present study. In fact, the addition of iron to NiOOH was found to improve the OER current density by 500-fold.[64] However, the contribution of manganese to the catalysis is non-trivial. Li *et al*. prepared Co_2P and CoMnP nanoparticles for OER catalysts finding that substituting Mn for Co lowered the overpotential for a current density of 10 mA cm^{-2} from 0.37 V to 0.33 V and decreased the Tafel slope from 128 mV dec^{-1} to 61 mV dec^{-1}.[24] Substitution of Mn for Fe in Fe_3O_4 was also found to greatly improve the material's electrocatalytic OER performance.[65] Moreover, MnO_2 as an OER electrocatalyst was reported to "self-heal" during operation in acidic and alkaline conditions with no observed mass loss.[66] Thus, an exact determination of which metal is active is elusive, but synergy likely arises from the bimetallic nature of the surface layer with a further contribution to stability arising from the presence of the manganese. This conclusion is further supported by comparison with the electrochemical performance of Fe_2P which requires an overpotential of 390 mV for 10 mA cm^{-2} for OER as reported by Read *et al.*, a full 90 mV higher than that required by FeMnP for the same current density.[67] Furthermore, Li *et al*. found that MnP nanoparticles quickly fade in performance concomitant with oxidation.[24]

Importantly, however, catalysis at the metal hydroxide/oxyhydroxide surface layer is fed by EC or PEC current supplied from the pristine, conductive FeMnP layer from which it seamlessly grew. It should be noted that the overpotentials exhibited in this work are much lower than even the lowest overpotentials of the metal layered-double hydroxides, likely due to the thinness of the oxidized layer through which the charge must traverse to perform the catalysis.

Although many new materials have been developed and identified as active electrocatalysts, it remains challenging to couple them with suitable semiconductors for PEC or photocatalytic water splitting. This is particularly true for TMPs. The common routes for TMPs like the solvothermal method using P_{red}, P_4, or Na_3P and metal chloride,[68] or thermal phosphidation using either *in situ* generated PH_3 or trioctylphosphine,[69] are too destructive for semiconductor substrates. These methods have limited phase control over the metal-phosphorus stoichiometries resulting in inhomogeneities. Moreover, existing methods cannot guarantee complete coverage of the metal phosphide over the semiconductor surface. The most similar technique in terms of substrate coverage is Atomic-Layer Deposition (ALD), but metal phosphide deposition has not been achieved to date by ALD, and such films would likely also suffer from poor phase control.

Past work in which Fe_3P, $(Fe_{1-x}Co_x)_3P$, and $Fe_3(P_{1-x}Te_x)$ thin films were grown on quartz substrates by MOCVD using organometallic precursors has established a simple route to growing TMP films at mild temperature.[36,37] In the present work, we applied our method to grow a TMP film directly on a semiconductor surface. The MOCVD method employed for FeMnP demonstrates its advantageousness in the fabrication of a highly active photoanode with a semiconductor/electrocatalyst three-dimensional core/shell architecture. The fast, low temperature MOCVD process has no negative effects on the TiO_2 substrate. The volatility of the specifically designed and synthesized single-source precursor ensures the uniform coating of FeMnP on TiO_2. The preliminary results in this work demonstrate the great potential of the present single-source MOCVD method in the integration of semiconductor and electrocatalyst for solar water splitting. Moreover given the availability of other main group element-containing homo- and heterometallic carbonyl clusters,[41,70] the MOCVD technique should prove generally

applicable for deposition of other electrocatalysts from single-source precursors onto semiconductors for the development of various highly active photoelectrodes.

CONCLUSIONS

In this work, we reported a ternary, metallic phosphide FeMnP electrocatalyst prepared by a single-source MOCVD method. It is demonstrated that FeMnP is an efficient OER electrocatalyst which can deliver an overpotential of 300 mV to reach a current density of 10 mA cm^{-2} with the low Tafel slope of 65 mV dec^{-1}. FeMnP also displayed excellent stability in strong base for OER. FeMnP was then uniformly deposited onto the 3D TiO_2 nanorod array to form a core/shell nanostructure photoanode. The as-fabricated TiO_2/FeMnP core/shell nanorod photoanode displayed significantly enhanced PEC performance. The photocurrent density is close to the theoretical value of rutile TiO_2 under 100 mW cm^{-2} irradiation. FeMnP also negatively shifted the photocurrent onset potential by about 200 mV. The high PEC performance is attributed to the high catalytic activity of FeMnP. The formation of a high quality interfacial junction between the TiO_2 light absorber and the FeMnP electrocatalyst is crucial for promoting interfacial hole transfer to the active metal oxyhydroxide surface. It is found that the metallic FeMnP interlayer between the semiconductor core and surface active sites plays an important role in the suppression of charge recombination and promotion of charge transfer. The present MOCVD method provides a facile strategy to couple efficient electrocatalysts with semiconductor photoanodes for photoelectrochemical solar energy conversion.

MATERIALS AND METHODS

Chemicals and Materials. Titanium butoxide (Sigma-Aldrich), Hydrochloric acid (37%, Sigma-Aldrich), Sodium hydroxide (Sigma-Aldrich), Potassium Hydroxide (Sigma-Aldrich). FTO glass (TEC 7, with resistivity of 6-8 Ω cm^{-2}) was obtained from Hartford Glass Co. $FeMn(CO)_8(\mu\text{-}PH_2)$ was synthesized according to previous work.[39]

Synthesis of TiO_2 nanorod array. TiO_2 nanorod arrays on fluorine-doped tin oxide (FTO) were grown through a hydrothermal process. In a typical procedure, 0.25 mL of titanium butoxide was added to 7.5 mL of concentrated HCl (35%), followed by the addition of 7.5 mL deionized water. The above solution was then transferred into an autoclave with a capacity of 50 mL. Two pieces of FTO substrate were placed into the autoclave at an angle with the conductive side facing down. The autoclave was then heated to 150 ^oC for 24 hours in an electric oven. After the growth, the FTO substrates were rinsed copiously with deionized water and ethanol. Then the FTO with TiO_2 nanorod array was dried at 70 ^oC for 6 h, followed by calcination at 500 ^oC for 2 h at a rate of 5 ^oC min^{-1}.

Synthesis of TiO_2/FeMnP core/shell nanorod array and FeMnP/FTO. FeMnP was deposited with a modified literature procedure.[38] The custom, home-built MOCVD apparatus employed in this work consists of a quartz tube of inner diameter 22 mm equipped with a Kimble-Chase high vacuum valve at the end furthest from the precursor and capped with a size 25 o-ring joint/cap assembly. 15 mm^2 substrates (TiO_2/FTO) were affixed to the stainless steel heating stage with silver paste and heated at 130 ^oC in air to cure the silver paste and provide good thermal contact. The precursor $FeMn(CO)_8(\mu\text{-}PH_2)$ was loaded in a glove box under a nitrogen atmosphere. The substrate-affixed heating stage was placed in the apparatus and sealed. It was transferred to a high-vacuum manifold and the end of the apparatus with the precursor was submerged in a liquid nitrogen bath. While the precursor was kept at 77 K, the apparatus was evacuated until a cold-

cathode ionization vacuum gauge stabilized at approximately 2×10^{-6} Torr. The position of the heating stage in the apparatus was adjusted to achieve optimum substrate coverage (**Figure S1**). Zone 1 of the apparatus, where the substrates were located, was then heated to 350 °C for 30 minutes using heating tape. The nitrogen bath was removed from the precursor and the precursor was allowed to warm to room temperature. After 20 minutes, a metallic film had formed on the substrates and walls surrounding the substrate assembly. The apparatus was disassembled under nitrogen and the material stored in air. FeMnP was deposited onto bare FTO with the same procedure by replacing the TiO_2/FTO substrate with bare FTO with 20 mg of precursor.

Material Characterization. Scanning electron microscopy (SEM) images were collected with an FEI XL-30FEG. The XRD characterization was conducted on a SIEMENS Diffractometer D5000 equipped with a Cu target. Transmission electron microscope (TEM), high-resolution transmission electron microscope (HRTEM) and energy dispersive X-ray spectroscopy (EDS) were performed by utilizing a JEM JEOL-2010F electron microscope. UV-VIS spectra was recorded with a HITARCHI spectroscopy U-2100. X-Ray photoelectron spectroscopy (XPS) was carried out on a Physical Electronics PHI Quantera SXM instrument using a monochromatic Al Kα source (1486.6 eV) operated at 40.7 W with a beam size of 200 μm and a take-off angle of 45°. Sputtering was performed with a 2 mm by 2 mm 3keV Ar^+ ion beam with 0.5 mA current. Weight measurements were performed on a Mettler –Toledo AX105 scale, accurate to ±0.01mg. FeMnP deposition amounts (mg cm^{-2}) were determined by weighing the substrate before and after deposition.

Electrochemical (EC) measurements. The electrochemical measurements were conducted on a 263A Princeton Applied Research (PAR) potentialstat/galvanostat Instrument. The FeMnP/FTO sample was wired using a copper wire with silver colloid paste. Epoxy was applied and solidified

to cover the FTO substrate, the silver paste, and wire to avoid short circuit. Finally, the FeMnP/FTO electrode was used as the working electrode. A Pt plate was employed as the counter electrode and Ag|AgCl as the reference electrode. A 1.0 M KOH aqueous solution was used as the electrolytic medium and bubbled with N_2 for 30 min prior to measurement. The linear sweep voltammetry (LSV) was measured at a scan rate of 10 mV s^{-1}. The electrolyte was continuously bubbled with N_2 during the measurement. The potential *versus* that of the reversible hydrogen electrode (RHE) was calculated with a reference to Ag|AgCl according to the Nernst equation:

$$E_{RHE} = E_{Ag|AgCl} + 0.05916 \times pH + E_0 \quad (1)$$

Where E_{RHE} is the potential *vs* reference hydrogen electrode (RHE), $E_{Ag|AgCl}$ is the measured potential *vs* Ag|AgCl, and E_0 = 0.2 V at 25 ^oC. The electrochemical impedance spectra (EIS) were recorded over a range from 10 KHz to 10 mHz with an AC amplitude of 10 mV. The cyclic voltammograms (CVs) were conducted in the non-Faradaic potential range of -0.35 V to -0.25 V *vs* Ag|AgCl at scan rates of 10 mV s^{-1}, 30 mV s^{-1}, 50 mV s^{-1}, 70 mV s^{-1} and 90 mV s^{-1}, for the measurement of the electrochemically active surface area (ECSA). The stability was evaluated by conducting the CV scans for 1000 cycles at 100 mV s^{-1} in the range of -0.2 V to 0.7 V *vs* Ag|AgCl. The Faradaic efficiency was determined by comparing the amount of experimentally produced O_2 during water electrolysis to the amount of theoretically calculated O_2. Water electrolysis was performed in an airtight electrochemical cell in 1 M KOH at overpotential of 300 mV using FeMnP/FTO and Pt as the working and the counter electrode, respectively. Before reaction, the electrolyte was degassed with N_2 and the produced O_2 was analyzed by a gas chromatograph (GC) which was calibrated with highly pure O_2 in advance.

Photoelectrochemical (PEC) measurements

The preparation of the photoelectrodes was similar to that of FeMnP/FTO electrode in the EC measurements. A photoelectrochemical cell (PEC) with a three-electrode configuration was used. In the PEC measurements, the Pt plate and Ag|AgCl were used as the counter electrode and reference electrode, respectively. PEC performance was measured in 0.5 M NaOH aqueous electrolyte which was bubbled with N_2 for 30 min prior to measurement. All photoelectrodes were illuminated from the back side. The loading amount of FeMnP on TiO_2 nanorod was adjusted by changing the amount of precursor. The SEM images of TiO_2/FeMnP core/shell samples with different amount of precursors (2 mg, 5 mg, 10 mg and 20 mg) are shown in **Figure S14**. We found that the sample prepared from 20 mg precursor showed the highest photocurrent density at 1.23 V *vs* RHE. Therefore, in this work, all the PEC measurements were conducted by using the sample prepared from 20 mg precursors. A commercial solar simulator (300 W, Newport) equipped with a Xenon lamp and an AM 1.5G filter was used as the light source in all measurements. The J-V curves were recorded at a scan rate of 10 mV s^{-1}. The ON-OFF curves were obtained at 1.23 V *vs* RHE (0.228 V *vs* Ag|AgCl). The photo-to-electric conversion efficiency (η) was calculated according to the equation:

$$\eta = J \times (1.23 - E_{RHE})/P_{light} \qquad (2)$$

Where J is the photocurrent density at the measured potential and P_{light} is the irradiation intensity of 100 mW/cm^2. The Nyquist plots of the photoelectrodes were obtained from AC impedance measurements performed at an AC amplitude of 10 mV at the frequency range of 10 KHz to 10 mHz at 1.23 V *vs* RHE with simulated solar light illuminated from the back side. Mott-Schottky plots were obtained with a three-electrode set-up at a preset frequency using an AC amplitude of 10 mV in the dark. The densities of charge carriers were obtained according to the equation:[70]

$$N_D = (2/e\varepsilon\varepsilon_0)\left[d\frac{1}{C^2}/dV\right]^{-1} \qquad (3)$$

Where N_D is the donor density (electron donor concentration for n-type semiconductor or hole acceptor concentration for p-type semiconductor), ε is the dielectric constant of the semiconductor (170 for rutile TiO_2),[71] ε_0 is the permittivity of free space (8.854×10^{-12} F m^{-1}), and e is the electron charge of 1.602×10^{-19} C.

Work function measurements. The work function of FeMnP/FTO and bare FTO was measured by a Kelvin probe S (Bescocke Delta Phi) equipped with a source meter in vacuum. A gold probe with a reference work function of 5.10 eV was used for the measurement. At constant interval, the contact potential difference (CPD) was recorded. The work function was then calculated by equation:

$$\Phi = \text{CPD} + 5.10 \text{ eV} \quad (4)$$

ASSOCIATED CONTENT

Supporting Information.

A pdf file (17 pages) containing the following information: Diagram of the MOCVD apparatus; SEM image of bare TiO_2 nanorod array on FTO substrate; XRD of TiO_2/FeMnP core/shell nanorod array on FTO substrate; SEM of FeMnP on FTO substrate; Comparison of OER activity of single phase catalysts (Table); Nyquist plot of FeMnP/FTO electrode at overpotential of 300 mV in 1.0 M KOH; Measurements of the electrochemically active surface area (ECSA) of FeMnP on FTO substrate; Time dependence of catalytic current density of FeMnP/FTO electrode in 1.0 M KOH at overpotential of 300 mV; the Faradaic efficiency (experimentally produced O_2 *versus* theoretically calculated amount of O_2); UV-VIS spectra of TiO_2 nanorod array on FTO glass showing the light absorption edge of 400 nm with

corresponding Tauc plot; Transmittance of TiO_2 and TiO_2/FeMnP; Comparison of photoanodes under simulated light irradiation of100 mW cm^{-2} (Table); Sputtering assisted XPS spectra of the TiO_2/FeMnP core/shell nanorod after stability test; Nyquist plots of the TiO_2 and TiO_2/FeMnP core/shell nanorod photoanodes at 1.23 V *vs* RHE under light irradiation; Work function of FeMnP/FTO and bare FTO; SEM image at different magnifications of TiO_2/FeMnP core/shell nanorod array after stability test; SEM images of TiO_2/FeMnP core/shell nanorod arrays with different FeMnP loading amounts achieved by changing the amount of precursor. This material is available free of charge *via* the Internet at http://pubs.acs.org.

NOTES

The authors declare no competing financial interest.

ACKNOWLEDGMENTS

The authors thank Rice University, the National Science Foundation (CHE-1411495, KHW), and the Robert A. Welch Foundation (C-0976, KHW; E-1728, JB) for funding. This material is based upon work supported by the National Science Foundation Graduate Research Fellowship (DES) under Grant No. 1450681.

REFERENCES

(1) Armstrong, R. C.; Wolfram, C.; Jong, K. P. de; Gross, R.; Lewis, N. S.; Boardman, B.; Ragauskas, A. J.; Ehrhardt-Martinez, K.; Crabtree, G.; Ramana, M. V. The Frontiers of Energy. *Nat. Energy* **2016**, *1*, 15020.

(2) Shaner, M. R.; Atwater, H. A.; Lewis, N. S.; McFarland, E. W. A Comparative Technoeconomic Analysis of Renewable Hydrogen Production Using Solar Energy. *Energy Environ. Sci.* **2016**, *9*, 2354–2371.

(3) Li, J.; Wu, N. Semiconductor-Based Photocatalysts and Photoelectrochemical Cells for Solar Fuel Generation: A Review. *Catal. Sci. Technol.* **2015**, *5*, 1360–1384.

(4) Yang, J.; Wang, D.; Han, H.; Li, C. Roles of Cocatalysts in Photocatalysis and Photoelectrocatalysis. *Acc. Chem. Res.* **2013**, *46*, 1900–1909.

(5) Sun, K.; Liu, R.; Chen, Y.; Verlage, E.; Lewis, N. S.; Xiang, C. A Stabilized, Intrinsically Safe, 10% Efficient, Solar-Driven Water-Splitting Cell Incorporating Earth-Abundant Electrocatalysts with Steady-State pH Gradients and Product Separation Enabled by a Bipolar Membrane. *Adv. Energy Mater.* **2016**, *6*, 1600379.

(6) Hunter, B. M.; Gray, H. B.; Müller, A. M. Earth-Abundant Heterogeneous Water Oxidation Catalysts. *Chem. Rev.* **2016**, *116*, 14120–14136.

(7) Roger, I.; Shipman, M. A.; Symes, M. D. Earth-Abundant Catalysts for Electrochemical and Photoelectrochemical Water Splitting. *Nat. Rev. Chem.* **2017**, *1*, 0003.

(8) Zhu, Y. P.; Guo, C.; Zheng, Y.; Qiao, S.-Z. Surface and Interface Engineering of Noble-Metal-Free Electrocatalysts for Efficient Energy Conversion Processes. *Acc. Chem. Res.* **2017**.

(9) Wang, D.; Astruc, D. The Recent Development of Efficient Earth-Abundant Transition-Metal Nanocatalysts. *Chem. Soc. Rev.* **2017**, *46*, 816–854.

(10) Xiang, C. X.; Papadantonakis, K. M.; Lewis, N. S. Principles and Implementations of Electrolysis Systems for Water Splitting. *Mater. Horiz.* **2016**, *3*, 169–173.

(11) Govindaraju, G. V.; Wheeler, G. P.; Lee, D.; Choi, K.-S. Methods for Electrochemical Synthesis and Photoelectrochemical Characterization for Photoelectrodes. *Chem. Mater.* **2017**, *29*, 355–370.

(12) Kibsgaard, J.; Tsai, C.; Chan, K.; Benck, J. D.; Norskov, J. K.; Abild-Pedersen, F.; Jaramillo, T. F. Designing an Improved Transition Metal Phosphide Catalyst for Hydrogen Evolution Using Experimental and Theoretical Trends. *Energy Environ. Sci.* **2015**, *8*, 3022–3029.

(13) Xiao, P.; Chen, W.; Wang, X. A Review of Phosphide-Based Materials for Electrocatalytic Hydrogen Evolution. *Adv. Energy Mater.* **2015**, *5*, n/a-n/a.

(14) Callejas, J. F.; Read, C. G.; Roske, C. W.; Lewis, N. S.; Schaak, R. E. Synthesis, Characterization, and Properties of Metal Phosphide Catalysts for the Hydrogen-Evolution Reaction. *Chem. Mater.* **2016**, *28*, 6017–6044.

(15) Shi, Y.; Zhang, B. Recent Advances in Transition Metal Phosphide Nanomaterials: Synthesis and Applications in Hydrogen Evolution Reaction. *Chem. Soc. Rev.* **2016**, *45*, 1529–1541.

(16) Stern, L.-A.; Feng, L.; Song, F.; Hu, X. Ni_2P as a Janus Catalyst for Water Splitting: The Oxygen Evolution Activity of Ni_2P Nanoparticles. *Energy Environ. Sci.* **2015**, *8*, 2347–2351.

(17) Yang, X.; Lu, A.-Y.; Zhu, Y.; Min, S.; Hedhili, M. N.; Han, Y.; Huang, K.-W.; Li, L.-J. Rugae-like FeP Nanocrystal Assembly on a Carbon Cloth: An Exceptionally Efficient and Stable Cathode for Hydrogen Evolution. *Nanoscale* **2015**, *7*, 10974–10981.

(18) Zhang, Z.; Lu, B.; Hao, J.; Yang, W.; Tang, J. FeP Nanoparticles Grown on Graphene Sheets as Highly Active Non-Precious-Metal Electrocatalysts for Hydrogen Evolution Reaction. *Chem. Commun.* **2014**, *50*, 11554–11557.

(19) Jiang, P.; Liu, Q.; Liang, Y.; Tian, J.; Asiri, A. M.; Sun, X. A Cost-Effective 3D Hydrogen Evolution Cathode with High Catalytic Activity: FeP Nanowire Array as the Active Phase. *Angew. Chem. Int. Ed.* **2014**, *53*, 12855–12859.

(20) Zhu, Y.-P.; Liu, Y.-P.; Ren, T.-Z.; Yuan, Z.-Y. Self-Supported Cobalt Phosphide Mesoporous Nanorod Arrays: A Flexible and Bifunctional Electrode for Highly Active Electrocatalytic Water Reduction and Oxidation. *Adv. Funct. Mater.* **2015**, *25*, 7337–7347.

(21) Tang, C.; Zhang, R.; Lu, W.; He, L.; Jiang, X.; Asiri, A. M.; Sun, X. Fe-Doped CoP Nanoarray: A Monolithic Multifunctional Catalyst for Highly Efficient Hydrogen Generation. *Adv. Mater.* **2016**.

(22) Yu, X.; Zhang, S.; Li, C.; Zhu, C.; Chen, Y.; Gao, P.; Qi, L.; Zhang, X. Hollow CoP Nanoparticle/N-Doped Graphene Hybrids as Highly Active and Stable Bifunctional Catalysts for Full Water Splitting. *Nanoscale* **2016**, *8*, 10902–10907.

(23) Wang, X.-D.; Xu, Y.-F.; Rao, H.-S.; Xu, W.-J.; Chen, H.-Y.; Zhang, W.-X.; Kuang, D.-B.; Su, C.-Y. Novel Porous Molybdenum Tungsten Phosphide Hybrid Nanosheets on Carbon Cloth for Efficient Hydrogen Evolution. *Energy Environ. Sci.* **2016**, *9*, 1468–1475.

(24) Li, D.; Baydoun, H.; Verani, C. N.; Brock, S. L. Efficient Water Oxidation Using CoMnP Nanoparticles. *J. Am. Chem. Soc.* **2016**, *138*, 4006–4009.

(25) Tan, Y.; Wang, H.; Liu, P.; Shen, Y.; Cheng, C.; Hirata, A.; Fujita, T.; Tang, Z.; Chen, M. Versatile Nanoporous Bimetallic Phosphides towards Electrochemical Water Splitting. *Energy Environ. Sci.* **2016**, *9*, 2257–2261.

(26) Yu, J.; Li, Q.; Li, Y.; Xu, C.-Y.; Zhen, L.; Dravid, V. P.; Wu, J. Ternary Metal Phosphide with Triple-Layered Structure as a Low-Cost and Efficient Electrocatalyst for Bifunctional Water Splitting. *Adv. Funct. Mater.* **2016**, *26*, 7644–7651.

(27) Wang, C.; Jiang, J.; Ding, T.; Chen, G.; Xu, W.; Yang, Q. Monodisperse Ternary NiCoP Nanostructures as a Bifunctional Electrocatalyst for Both Hydrogen and Oxygen Evolution Reactions with Excellent Performance. *Adv. Mater. Interfaces* **2016**, *3*, 1500454.

(28) Ran, J.; Zhang, J.; Yu, J.; Jaroniec, M.; Qiao, S. Z. Earth-Abundant Cocatalysts for Semiconductor-Based Photocatalytic Water Splitting. *Chem. Soc. Rev.* **2014**, *43*, 7787–7812.

(29) Seabold, J. A.; Choi, K.-S. Effect of a Cobalt-Based Oxygen Evolution Catalyst on the Stability and the Selectivity of Photo-Oxidation Reactions of a WO_3 Photoanode. *Chem. Mater.* **2011**, *23*, 1105–1112.

(30) Park, Y.; J. McDonald, K.; Choi, K.-S. Progress in Bismuth Vanadate Photoanodes for Use in Solar Water Oxidation. *Chem. Soc. Rev.* **2013**, *42*, 2321–2337.

(31) Zhong, D. K.; Gamelin, D. R. Photoelectrochemical Water Oxidation by Cobalt Catalyst ("Co−Pi")/α-Fe_2O_3 Composite Photoanodes: Oxygen Evolution and Resolution of a Kinetic Bottleneck. *J. Am. Chem. Soc.* **2010**, *132*, 4202–4207.

(32) Xu, D.; Rui, Y.; Li, Y.; Zhang, Q.; Wang, H. Zn-Co Layered Double Hydroxide Modified Hematite Photoanode for Enhanced Photoelectrochemical Water Splitting. *Appl. Surf. Sci.* **2015**, *358*, *Part A*, 436–442.

(33) Sun, K.; Park, N.; Sun, Z.; Zhou, J.; Wang, J.; Pang, X.; Shen, S.; Noh, S. Y.; Jing, Y.; Jin, S. Nickel Oxide Functionalized Silicon for Efficient Photo-Oxidation of Water. *Energy Environ. Sci.* **2012**, *5*, 7872–7877.

(34) Le Formal, F.; Pendlebury, S. R.; Cornuz, M.; Tilley, S. D.; Grätzel, M.; Durrant, J. R. Back Electron–Hole Recombination in Hematite Photoanodes for Water Splitting. *J. Am. Chem. Soc.* **2014**, *136*, 2564–2574.

(35) Ma, Y.; Formal, F. L.; Kafizas, A.; R. Pendlebury, S.; R. Durrant, J. Efficient Suppression of Back Electron/Hole Recombination in Cobalt Phosphate Surface-Modified Undoped Bismuth Vanadate Photoanodes. *J. Mater. Chem. A* **2015**, *3*, 20649–20657.

(36) Colson, A. C.; Chen, C.-W.; Morosan, E.; Whitmire, K. H. Synthesis of Phase-Pure Ferromagnetic Fe_3P Films from Single-Source Molecular Precursors. *Adv. Funct. Mater.* **2012**, *22*, 1850–1855.

(37) Leitner, A. P.; Chen, J.-H.; Schipper, D. E.; Whitmire, K. H. Thin Films of $(Fe_{1-x}Co_x)_3P$ and $Fe_3(P_{1-x}Te_x)$ from the Co-Decomposition of Organometallic Precursors by MOCVD. *Chem. Mater.* **2016**, *28*, 7066–7071.

(38) Leitner, A. P.; Schipper, D. E.; Chen, J.-H.; Colson, A. C.; Rusakova, I.; Rai, B. K.; Morosan, E.; Whitmire, K. H. Synthesis of Hexagonal FeMnP Thin Films from a Single-Source Molecular Precursor. *Chem. - Eur. J.* **2017**, *In Press*.

(39) Colson, A. C.; Whitmire, K. H. Synthesis, Characterization, and Reactivity of the Heterometallic Dinuclear μ-PH_2 and μ-PPhH Complexes $FeMn(CO)_8$(μ-PH_2) and $FeMn(CO)_8$(μ-PPhH). *Organometallics* **2010**, *29*, 4611–4618.

(40) Li, J.; Wu, N. Semiconductor-Based Photocatalysts and Photoelectrochemical Cells for Solar Fuel Generation: A Review. *Catal. Sci. Technol.* **2015**.

(41) Whitmire, K. H. Main Group-Transition Metal Cluster Compounds of the Group 15 Elements. *Adv. Organomet. Chem.* **1998**, *42*, 2–146.

(42) Hwang, Y. J.; Hahn, C.; Liu, B.; Yang, P. Photoelectrochemical Properties of TiO_2 Nanowire Arrays: A Study of the Dependence on Length and Atomic Layer Deposition Coating. *ACS Nano* **2012**, *6*, 5060–5069.

(43) Powell, C. J. Recommended Auger Parameters for 42 Elemental Solids. *J. Electron Spectrosc. Relat. Phenom.* **2012**, *185*, 1–3.

(44) Di Castro, V.; Polzonetti, G. XPS Study of MnO Oxidation. *J. Electron Spectrosc. Relat. Phenom.* **1989**, *48*, 117–123.

(45) Mahan, J.; Vantomme, A. Trends in Sputter Yield Data in the Film Deposition Regime. *Phys. Rev. B* **2000**, *61*, 8516–8525.

(46) Ho, P. S.; Lewis, J. E.; Wildman, H. S.; Howard, J. K. Auger Study of Preferred Sputtering on Binary Alloy Surfaces. *Surf. Sci.* **1976**, *57*, 393–405.

(47) Hofmann, S. Sputter Depth Profile Analysis of Interfaces. *Rep. Prog. Phys.* **1998**, *61*, 827–888.

(48) Hofmann, S. Quantitative Depth Profiling in Surface Analysis: A Review. *Surf. Interface Anal.* **1980**, *2*, 148–160.

(49) Coburn, J. Sputtering in the Surface Analysis of Solids: A Discussion of Some Problems. *J. Vac. Sci. Technol.* **1976**, *13*, 1037.

(50) Werner, H. W.; Warmoltz, N. The Influence of Selective Sputtering on Surface Composition. *Surf. Sci.* **1976**, *57*, 706–714.

(51) Ramírez, A.; Hillebrand, P.; Stellmach, D.; May, M. M.; Bogdanoff, P.; Fiechter, S. Evaluation of MnO_x, Mn_2O_3, and Mn_3O_4 Electrodeposited Films for the Oxygen Evolution Reaction of Water. *J. Phys. Chem. C* **2014**, *118*, 14073–14081.

(52) Meng, Y.; Song, W.; Huang, H.; Ren, Z.; Chen, S.-Y.; Suib, S. L. Structure–Property Relationship of Bifunctional MnO_2 Nanostructures: Highly Efficient, Ultra-Stable Electrochemical Water Oxidation and Oxygen Reduction Reaction Catalysts Identified in Alkaline Media. *J. Am. Chem. Soc.* **2014**, *136*, 11452–11464.

(53) Fekete, M.; Hocking, R. K.; Chang, S. L. Y.; Italiano, C.; Patti, A. F.; Arena, F.; Spiccia, L. Highly Active Screen-Printed Electrocatalysts for Water Oxidation Based on β-Manganese Oxide. *Energy Env. Sci* **2013**, *6*, 2222.

(54) Ma, T.; Dai, S.; Jaroniec, M.; Qiao, S. Metal–Organic Framework Derived Hybrid Co_3O_4-Carbon Porous Nanowire Arrays as Reversible Oxygen Evolution Electrodes. *J. Am. Chem. Soc.* **2014**, *136*, 13925–13931.

(55) Tüysüz, H.; Hwang, Y. J.; Khan, S. B.; Asiri, A. M.; Yang, P. Mesoporous Co_3O_4 as an Electrocatalyst for Water Oxidation. *Nano Res.* **2012**, *6*, 47–54.

(56) Gao, M.-R.; Cao, X.; Gao, Q.; Xu, Y.-F.; Zheng, Y.-R.; Jiang, J.; Yu, S.-H. Nitrogen-Doped Graphene Supported $CoSe_2$ Nanobelt Composite Catalyst for Efficient Water Oxidation. *ACS Nano* **2014**, *8*, 3970–3978.

(57) McCrory, C. C. L.; Jung, S.; Peters, J. C.; Jaramillo, T. F. Benchmarking Heterogeneous Electrocatalysts for the Oxygen Evolution Reaction. *J. Am. Chem. Soc.* **2013**, *135*, 16977–16987.

(58) Li, J.; Cushing, S. K.; Zheng, P.; Meng, F.; Chu, D.; Wu, N. Plasmon-Induced Photonic and Energy-Transfer Enhancement of Solar Water Splitting by a Hematite Nanorod Array. *Nat. Commun.* **2013**, *4*, 2651.

(59) Paparazzo, E. XPS and Auger Spectroscopy Studies on Mixtures of the Oxides SiO_2, Al_2O_3, Fe_2O_3 and Cr_2O_3. *J. Electron Spectrosc. Relat. Phenom.* **1987**, *43*, 97–112.

(60) Tan, B. J.; Klabunde, K. J.; Sherwood, P. M. A. XPS Studies of Solvated Metal Atom Dispersed (SMAD) Catalysts. Evidence for Layered Cobalt-Manganese Particles on Alumina and Silica. *J. Am. Chem. Soc.* **1991**, *113*, 855–861.

(61) Dutta, A.; Pradhan, N. Developments of Metal Phosphides as Efficient OER Precatalysts. *J. Phys. Chem. Lett.* **2017**, *8*, 144–152.

(62) Helander, M. G.; Greiner, M. T.; Wang, Z. B.; Tang, W. M.; Lu, Z. H., Work Function of Fluorine Doped Tin Oxide. *J. Vac. Sci. Technol. A* **2011,** *29*, 011019.

(63) Burke, M. S.; Zou, S.; Enman, L. J.; Kellon, J. E.; Gabor, C. A.; Pledger, E.; Boettcher, S. W. Revised Oxygen Evolution Reaction Activity Trends for First-Row Transition-Metal (Oxy)hydroxides in Alkaline Media. *J. Phys. Chem. Lett.* **2015**, *6*, 3737–3742.

(64) Friebel, D.; Louie, M. W.; Bajdich, M.; Sanwald, K. E.; Cai, Y.; Wise, A. M.; Cheng, M.-J.; Sokaras, D.; Weng, T.-C.; Alonso-Mori, R.; Davis, R.C; Bargar, J.R.; Nørskov, J.K.; Nilsson, A.; Bell, A.T. Identification of Highly Active Fe Sites in (Ni,Fe)OOH for Electrocatalytic Water Splitting. *J. Am. Chem. Soc.* **2015**, *137*, 1305–1313.

(65) Singh, N. K.; Tiwari, S. K.; Anitha, K. L.; Singh, R. N. Electrocatalytic Properties of Spinel-Type $Mn_xFe_{3-x}O_4$ synthesized below 100 °C for Oxygen Evolution in KOH Solutions. *J. Chem. Soc., Faraday Trans.* **1996**, *92*, 2397–2400.

(66) Huynh, M.; Bediako, D. K.; Nocera, D. G. A Functionally Stable Manganese Oxide Oxygen Evolution Catalyst in Acid. *J. Am. Chem. Soc.* **2014**, *136*, 6002–6010.

(67) Read, C. G.; Callejas, J. F.; Holder, C. F.; Schaak, R. E. General Strategy for the Synthesis of Transition Metal Phosphide Films for Electrocatalytic Hydrogen and Oxygen Evolution. *ACS Appl. Mater. Interfaces* **2016**, *8*, 12798–12803.

(68) Brock, S. L.; Perera, S. C.; Stamm, K. L. Chemical Routes for Production of Transition-Metal Phosphides on the Nanoscale: Implications for Advanced Magnetic and Catalytic Materials. *Chem. – Eur. J.* **2004**, *10*, 3364–3371.

(69) Shi, Y.; Zhang, B. Recent Advances in Transition Metal Phosphide Nanomaterials: Synthesis and Applications in Hydrogen Evolution Reaction. *Chem. Soc. Rev.* **2016**, *45*, 1529–1541.

(70) Schipper, D. E.; Young, B. E.; Whitmire, K. H. Transformations in Transition-Metal Carbonyls Containing Arsenic: Exploring the Chemistry of $[Et_4N]_2[HAs\{Fe(CO)_4\}_3]$ in the

Search for Single-Source Precursors for Advanced Metal Pnictide Materials. *Organometallics* **2016**, *35*, 471–483.

Table of Contents Entry

Thin films of FeMnP deposited from the single-source precursor $FeMn(CO)_8(\mu\text{-}PH_2)$ onto TiO_2 nanorod arrays are found to be highly active for the photoelectrochemical oxygen evolution reaction (PEC-OER).